Direct Investigation of the Interparticle-based State-of-Charge Distribution of Polycrystalline NMC532 in Lithium-Ion Batteries by Classification-Single-Particle-ICP-OES

Till-Niklas Kröger<sup>a</sup>, Patrick Harte<sup>a</sup>, Sven Klein<sup>a</sup>, Thomas Beuse<sup>a</sup>, Markus Börner<sup>a</sup>, Martin Winter<sup>a,b</sup>, Sascha Nowak<sup>a</sup> and Simon Wiemers-Meyer<sup>a,\*</sup>

<sup>a</sup> University of Münster, MEET Battery Research Center, Corrensstraße 46, 48149 Münster, Germany

<sup>b</sup> Helmholtz-Institute Münster, IEK-12, FZ Jülich, Corrensstraße 46, 48149 Münster, Germany

\*Corresponding author: simon.wiemers-meyer@uni-muenster.de

#### **Abstract**

The presented case study provides mesoscopic insights into the state-of-charge (SOC) distribution of battery electrodes containing layered transition metal oxides with Li(Ni<sub>0.5</sub>Mn<sub>0.3</sub>Co<sub>0.2</sub>)O<sub>2</sub> (NMC532). The application of classification-single-particle inductively coupled plasma optical emission spectroscopy (CL-SP-ICP-OES) enables the rapid screening of the lithium content of individual cathode active material (CAM) particles achieving a statistically viable elucidation of the mesoscale SOC distribution between different particles of the electrode. The results reveal the evolution of a persistent mesoscale SOC heterogeneity of the electrode upon delithiation at slow rates and extensive relaxation times as confirmed by time-of-flight secondary ion mass spectrometry (ToF-SIMS). The implications of local chemical and structural ramifications of the investigated NMC532 for heterogeneous active material utilization are thoroughly discussed. Furthermore, it is found that the evolved SOC heterogeneity of the electrode is strongly dependent on the current density. The correlation to the decreased capacity utilization is further investigated with a straightforward quantification

approach revealing a considerable contribution to capacity fading by persistently inactive lithium in the CAM. The results highlight the importance of the analysis of persistent mesoscale SOC heterogeneity as a potential capacity fade mechanism in layered lithium transition metal oxide-based battery electrodes.

**Keywords:** Lithium ion batteries; Lithium transition metal oxides; State-of-charge heterogeneity; Single particle analysis; Aging mechanisms

#### 1. Introduction

Lithium ion battery (LIBs) cells are complex, hierarchically engineered functional devices with structural and chemical heterogeneity ubiquitously existing across a wide range of length scales in their components. This functional design is important for the energy storage and release mechanism since it is based on the coherent interplay of the different components enabling the shuttling of lithium ions between the electrodes and concomitant electron transfer outside the LIB cell. The most common positive electrode materials used in LIBs are lithium transition metal oxides LiMO<sub>2</sub> (M = Ni, Mn, Co, e.g. NMC532<sup>2</sup>), which consist of polycrystalline and heterogeneous particle ensembles embedded in a porous matrix of inactive components. <sup>1,3</sup> The mesoscale, namely the inter- and intraparticle level of electrodes is regarded as an area of utmost importance since the macroscopic behavior of the LIB originates from ramifications of its microscopic structure and chemical properties.<sup>1,4</sup> The local electrochemical environment is impacted by intrinsic properties of the electrode materials (e.g. particle morphology, size, porosity), ionic and electronic wiring as well as by interrelated physicochemical properties such as lithium diffusivity and electron conductivity.<sup>1,5–9</sup> Structural and thereto related chemical heterogeneity significantly affects the mesoscale lithium transport pathways and ultimately leads to SOC heterogeneity on particle level. 10-12 During operation, this mesoscale SOC heterogeneity is potentially amplified by prolonged electrochemical cycling under different external stimuli (e.g. high C-rates). There are many side reactions contributing to the mesoscale SOC heterogeneity potentially leading to device failure, including surface reconstruction<sup>13,14</sup>, change of the electronic or ionic contact or domain deactivation by mechanical disintegration<sup>15-17</sup>. The intrinsic complexity of LIBs has led to a plethora of applied analytical techniques. As like other batteries, the LIB consists of several components including the electrolyte, separator and the electrodes<sup>18</sup>. Macroscale battery research is often based on ensemble techniques such as impedance spectroscopy or XRD providing statistical information on composite electrode level, 10 however, to unravel the SOC heterogeneity on particle level, analytical techniques are needed that can reveal chemical details in large sample volumes. For the investigation of the mesoscale battery chemistry of NMC-based electrode materials, X-ray X-ray based techniques hard spectroscopic such as soft and absorption spectroscopy (XAS)<sup>5,12,17,19–24</sup>, X-ray Raman spectroscopy (XRS)23–25, transmission X-ray microscopy  $(TXM)^{15-17,20-22,24-26}$  or X-ray tomography  $(XRT)^{21,23,27}$  are used most prevalently. These synchrotron-based techniques can obtain spatial resolution of tens of nanometers enabling surface-sensitive mappings and bulk information of the SOC distribution in CAM particles. The investigation of the SOC in NMCs is primarily based on the Ni oxidation-state distribution as a proxy for the (de)lithiation during charge and discharge. However, the Ni redox is not always correlated directly to the alteration of the lithium content. Additional oxidation processes in NMCs of the redox couple Co<sup>3+</sup>/Co<sup>4+</sup> between potentials of 4.4 and 4.6 V vs. Li/Li<sup>+28,29</sup> or spatial variation in the transition metal ratios<sup>30–32</sup> can interfere with the analysis of the SOC distribution based solely on Ni redox. Furthermore, the application of synchrotronbased techniques is limited by the required highly specialized instrumentation, entailing low prevalence in routine analytics. ToF-SIMS is an analytical surface-sensitive imaging technique that enables the direct investigation of mesoscale SOCs by mapping the Li nanoscale distribution within CAM particles.<sup>33,34</sup> However, the limited practicability of particle bulk analyses and the relatively small analysis region, which might not be representative of the entire electrode are drawbacks of this technique. In this work, we present a method than can effectively and efficiently augment the merits of these techniques and tackle the intrinsically complicated mesoscale battery chemistry of NMC-based electrode materials. This study creates a new methodology to investigate the mesoscale SOC distribution between different particles through measurements directly based on the lithium content of individual particles by means of CL-SP-ICP-OES.<sup>35</sup> CL-SP-ICP-OES enables rapid element-specific, multi-element information of entire individual CAM particles achieving statistically viable elucidation of the mesoscale SOC distribution of the electrode. Therefore, this method aims to leverage mesoscopic research of the SOC distribution in NMC-based electrode materials for routine analytics with widespread commercial ICP-OES. This work provides insight into the reasons of SOC heterogeneity of particles in battery electrodes and presents a straightforward quantification approach for the amount of trapped (deactivated/dead/immobile<sup>36</sup>) Li in electrochemically deactivated particles upon cycling with NMC532. For this, the influence of slow and fast cycling protocols on the evolving mesoscale SOC heterogeneity will be discussed. Furthermore, ToF-SIMS is applied to visualize the micro-structural and chemical heterogeneity at fine length scales complementing the understanding of the reasons for the origin of mesoscale SOC heterogeneity, while CL-SP-ICP-OES can provide information about its extent in the electrode.

#### 2. Results and discussion

## 2.1. Investigation of the mesoscale SOC heterogeneity between different particles upon delithiation

For the investigation of the mesoscale SOC distribution, the degree of lithiation (DOL) of individual CAM particles is determined. For this, the intensity ratio of Li to Mn (I(Li)/I(Mn)) is measured on single particle level with CL-SP-ICP-OES. Mn was chosen for analysis by reason of higher emission line intensity, which results in better limits of detection compared to Ni and Co<sup>35</sup>. The intensity ratios are further calibrated with a matrix-matched external calibration with differently lithiated NMC532 as obtained by electrochemical delithiation. The mean DOL of differently lithiated CAMs is determined after acidic microwave digestion with ICP-OES in the solution mode. In **Figure 1**, the relative histograms of the intensity ratios of pristine and electrochemically delithiated NMC532 particles are presented. The intensity ratios show a Gaussian distribution. The width of the distribution is affected by the measurement settings (e.g. gas flow rates and plasma properties) as discussed in our recent publication<sup>35</sup>. Another possible reason influencing the distribution of the I(Li)/I(Mn) ratios are local inhomogeneities in the elemental composition, which are reported for synthesis approaches based on co-precipitated precursors most commonly used for NMC-based electrode materials<sup>37</sup>. It can be observed that after electrochemical delithiation the mean intensity ratio decreases as obtained by fitting the histogram with a Gaussian function. In Figure S1, it is shown that the mean intensity ratios decrease linearly with lower mean DOLs demonstrating the fundamental applicability of this calibration approach. Furthermore, the intrinsic structural and chemical complexities emphasize the need for matrix-matching of the calibration to compensate for potential effects that influence analytical response. Although matrix delithiation (e.g. with NO<sub>2</sub>BF<sub>4</sub>, Br<sub>2</sub>) has also been reported in literature, the electrolyte and the inactive components of the composite electrode play an important role in affecting the local chemistry of the CAM particles and need to be considered, which suggests the application of the electrochemical approach on real battery electrodes. 12,21–23,38

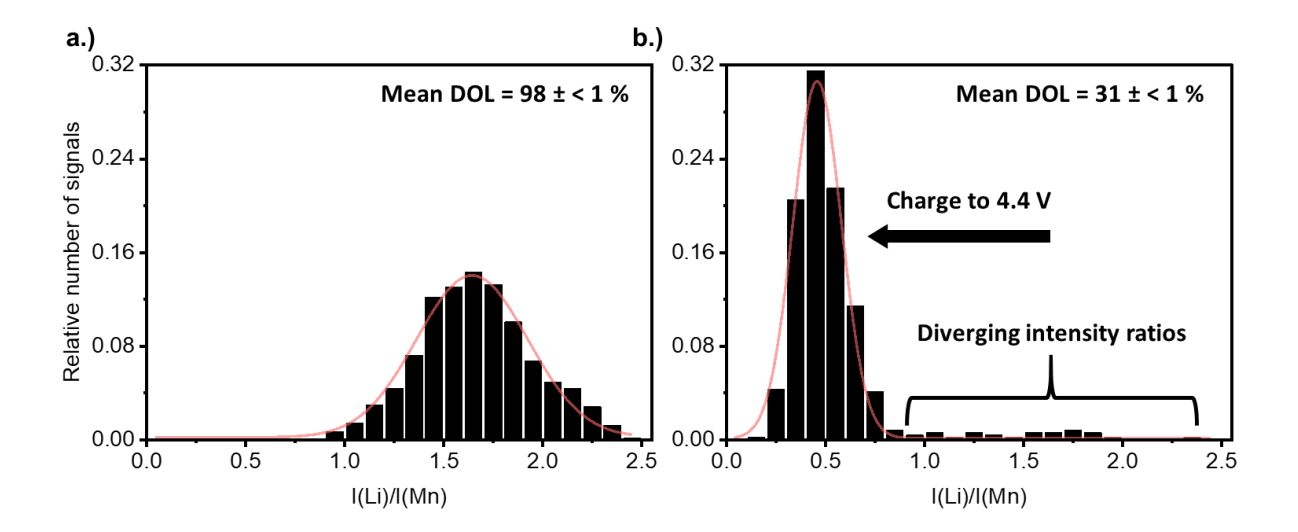


**Figure 1.** Relative histograms of the CAM particle intensity ratios in NMC532 $\parallel$ graphite cells (two-electrode configuration) of a.) pristine and b.) electrochemically delithiated NMC532 (SOC of 81  $\pm$  1 %) with the mean DOL as obtained by CL-SP-ICP-OES and after acidic microwave digestion with ICP-OES in solution mode, respectively.

It can be observed in **Figure 1** that the electrochemically delithiated NMC532 reveals particles with higher intensity ratios. On the assumption that the Li is uniformly delithiated, all the measured intensity ratios of the CAM particles are expected to be similar and to follow a Gaussian distribution. Therefore, the occurrence of the irregularly distributed intensity ratios in this range implies a non-uniform delithiation of the CAM, which potentially indicates an evolved mesoscale SOC heterogeneity. It is important to note that incompletely delithiated CAM particles can be detected due to diverging DOLs leading to different intensity ratios of individual particles. For electrochemical delithiation, slow rates and extensive relaxation times were applied to exclude large overpotentials and kinetically driven SOC heterogeneity. Although the heterogeneities in the (de)lithiation pathways are generally assumed to be transient since layered oxides such as NMC532 exhibit solid-solution phase behavior indicated

by sloping voltage profiles (**Figure S3**) and reasonable Li diffusivity<sup>39,40</sup>, the results underline the persistent nature of the emerged SOC heterogeneity contrary to the prevailing understanding.

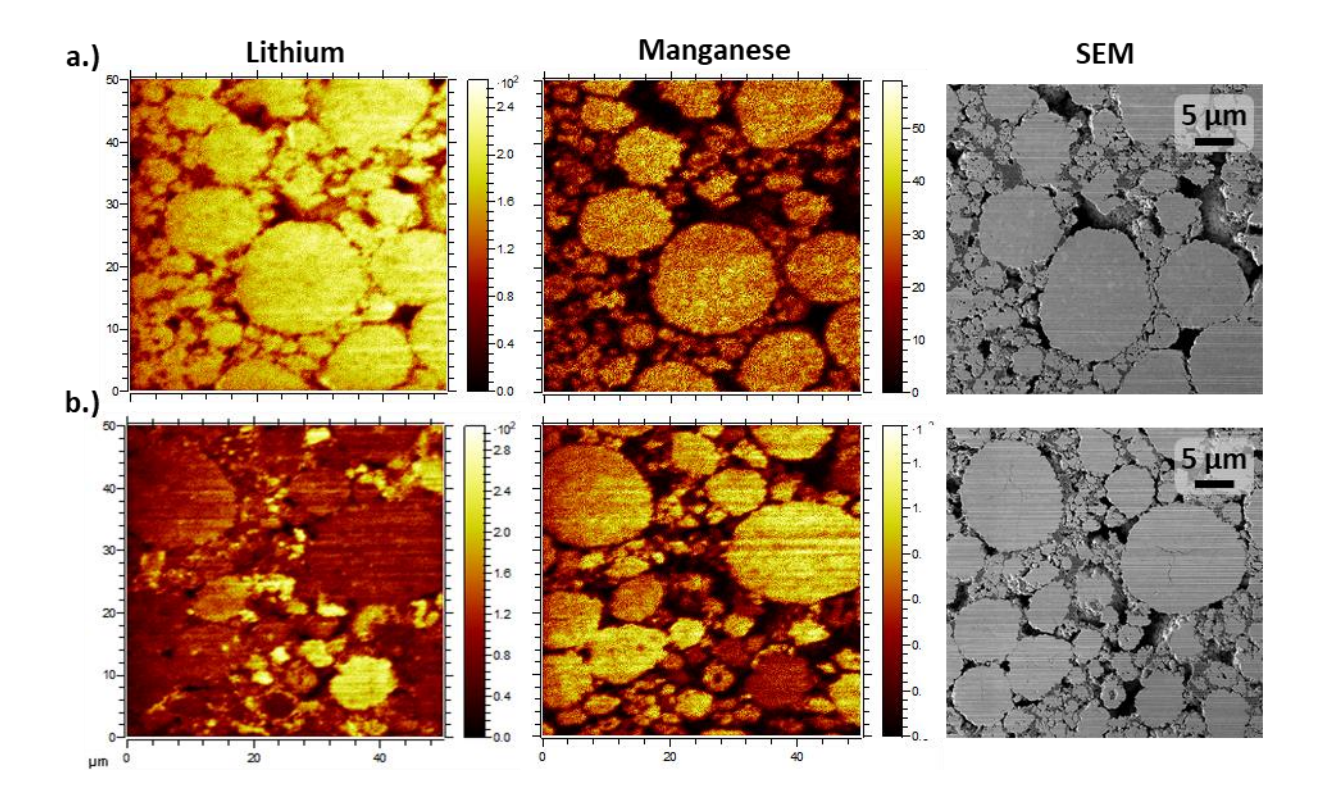


**Figure 2.** ToF-SIMS mappings for a FIB-prepared cross-sections of a.) pristine and b.) electrochemically delithiated NMC532 electrodes (SOC of  $81 \pm 1$  %). SEM and secondary ion images for Li-species ( $^6\text{Li}^+$ ,  $^7\text{Li}^+$ ) and  $^{55}\text{Mn}^+$  are presented.

To profoundly understand the reasons for the origin of the mesoscale SOC heterogeneity, the micro-structural and chemical heterogeneity at fine length scales need to be investigated complementary by ToF-SIMS, SEM and EDX. ToF-SIMS enables the investigation of the local electrochemical environment on the mesoscale by mapping the elemental distribution of Li with nanoscale lateral resolution. In **Figure 2**, the ToF-SIMS mappings of the cross-sectional lithium and manganese distribution of pristine and electrochemically delithiated NMC532 electrodes are presented. The cross-section of the pristine NMC532 electrode is characterized by a uniform Li distribution indicating a homogeneous mesoscale SOC distribution. On the other hand, the

Mn distribution of the pristine electrode appears to be size-dependent with lower intensities for smaller particles. Although ToF-SIMS is a powerful qualitative technique, quantitative information is severely compromised due to complex matrix effects. 41,42 Therefore, EDX was further used to obtain semi-quantitative information on the sample composition demonstrating the Mn distribution to be homogeneous and independent of the particle size (see discussion of Figure S4 and Table S1 in the supporting information). The cross-sectional Li distribution in the ToF-SIMS mapping after electrochemical delithiation is heterogeneous further evidencing non-uniform active material utilization. The unexpected heterogeneity of the Mn distribution in the ToF-SIMS mapping of the electrochemically delithiated NMC532 can be assigned to matrix effects, which are explained in detail in the supporting information (see discussion of Figure S5). To further investigate the emerged mesoscale SOC heterogeneity of the CAM particles, region of interest (ROI) analysis of the ToF-SIMS spectra is applied. In Figure S6, selected ROIs of individual delithiated (ROI 1) active material particles of the electrochemically delithiated and of the pristine (ROI 2) NMC532 electrode are presented. The similar intensities of Li in ROI1 and ROI2 corroborate the presence of trapped Li in electrochemically inactive particles. Furthermore, CAM particles with partial delithiation are observed in the ToF-SIMS mapping. These findings confirm the CL-SP-ICP-OES results and are in contrast to the expectation of uniform active material utilization during delithiation. The irregularly distributed intensity ratios account for  $6 \pm 1$  % of the total measured CAM particles in the investigated particle size range (Figure S2) as obtained with CL-SP-ICP-OES. This result demonstrates the extent of the mesoscale SOC heterogeneity upon delithiation for the investigated CAM and further explains the need for analytical diagnostic of the mesoscale. Furthermore, the potential of CL-SP-ICP-OES for complementing ToF-SIMS analysis by achieving statistically viable elucidation of the mesoscale SOC distribution of the electrode is highlighted. As discussed above, there are many conceivable reasons for the evolution of the mesoscale SOC heterogeneity. However, the occurrence of completely non-delithiated active material particles suggests their isolation from the ionic and/or electronic network of the composite electrode. The impeded lithium and electron transport potentially explain the persistence of the local potential differences that would drive the equilibration of the mesoscale SOC heterogeneity upon relaxation. The layered oxide active electrode materials suffer from poor electronic conductivity. Therefore, these materials are typically embedded into a matrix of highly conductive carbon materials that can effectively enhance electronic percolation. Carbon black is the most commonly used conductive agent for layered oxide electrode materials.

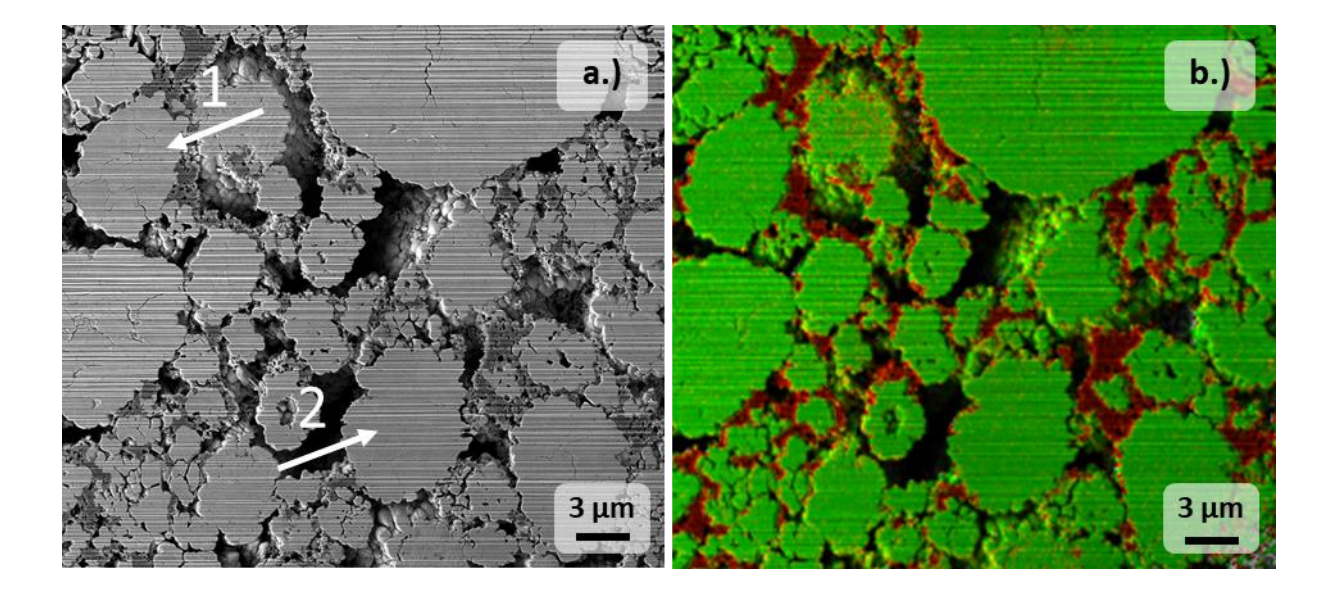


**Figure 3.** Magnified section of the FIB-prepared cross-section of an electrochemically delithiated NMC532 electrode (SOC of  $81 \pm 1$  %) with a.) a SEM image and b.) the EDX elemental mapping. For the EDX, an overlay of carbon (red) and oxygen (green) for better visualization of the conductive agent is presented. Exemplary active material particles with partial delithiation (1) and no delithiation (2) are highlighted in the SEM image as investigated by ToF-SIMS.

The carbon black nanoparticles form agglomerates in the active material interspaces facilitating the electronic conductivity by point-to-point contact between the carbon and the active material.<sup>44</sup> In **Figure 3**, the EDX elemental mapping of the carbon network as a proxy for the

electronic pathways is presented. It can be observed that the active material particles are not homogeneously covered with carbon black particles, which results in complex and convoluted transport pathways for the electrons implicated in the charge-transfer reaction and potentially long transport distances through the NMC532 particles. However, it needs to be emphasized that the investigated cross-section does not provide information about the three-dimensional connections of the conductive carbon matrix. Although the first highlighted particle is wellcontacted with conductive agent, the second particle exhibits a very low degree of carbon black coverage. Furthermore, the second particle exhibits severe cracking at the periphery implying the structural disintegration to the adjacent particles and minor cracking in the interior of the secondary particle (magnification in **Figure S7**). A possible reason for the peripheral and inner cracking is the local microscopic stress that emerges in the calandering process to control the porosity of the electrode during fabrication. 45,46 The development of microscopic cracks can cause transport barriers, which hinder the Li and electron transport rendering the particle to be electrochemically inactive. 1,8,47 The structural degradation of polycrystalline particles is also reported to arise from the electro-chemo-mechanical interplay leading to the formation of micro-cracks upon cycling. 48–50 The strong delithiation is accompanied by an anisotropic volume change of the lattice leading to the build-up of internal microscopic stress due to the randomly oriented primary particles in the secondary particle architecture. 47,48 In particular for the particle marked with number 1 in **Figure 3**, severe micro-cracking in the particle interior (magnification in Figure S7) and non-uniform delithiation (Figure 2) is observed. This indicates that the evolution of microscopic cracks during cycling can further cause kinetic hindrances for Li and electron transport, which potentially explains the heterogeneous delithiation. 1,8,47 However, the micro-cracks also provide further channels for electrolyte penetration into the particle interior, which can lead to new electrochemically active surface areas promoting improved Li transport kinetics. 50,51 The electrolyte wetting of the newly exposed surfaces changes the ion transport pathways but does not impact the electron transport kinetics due to electronic insulation, which potentially leads to a detouring of electron transport in the secondary particle. <sup>27,51,52</sup> The ionic contact of the CAM particles is generally ensured by the percolation of the electrolyte providing an interconnected transport network for the Li ions. Non-uniform exposure of electrolyte to the active material particles could significantly impede the (de)lithiation. However, an insufficient wetting of individual particles is unlikely a possible explanation for the observed electrochemical inactivity. In the case of poor active material wetting, inactive domains of multiple particles would be expected

# 2.2. Investigation of the mesoscale SOC heterogeneity between different particles upon cycling with different charging protocols

During electrochemical cycling, the macroscale SOC of the positive electrode changes perpetual with (de)lithiation as given by the electrode potential. On the mesoscale, this results in the continuous (de)lithiation of the CAM particles depending on the local potentials. As discussed above, the local electrochemistry is defined by the structural and chemical heterogeneity of the micro-environment, which in the case of electrochemical inactivation of CAM particles can lead to different potentials at the meso- and macroscale. The mismatching local electrochemical characteristic is a possible explanation for the mesoscale SOC heterogeneity of layered oxides and reported to be further amplified for high cycling rates. <sup>16,17,27</sup> Therefore, the evolution of the mesoscale SOC heterogeneity is investigated upon different charging protocols by means of CL-SP-ICP-OES.

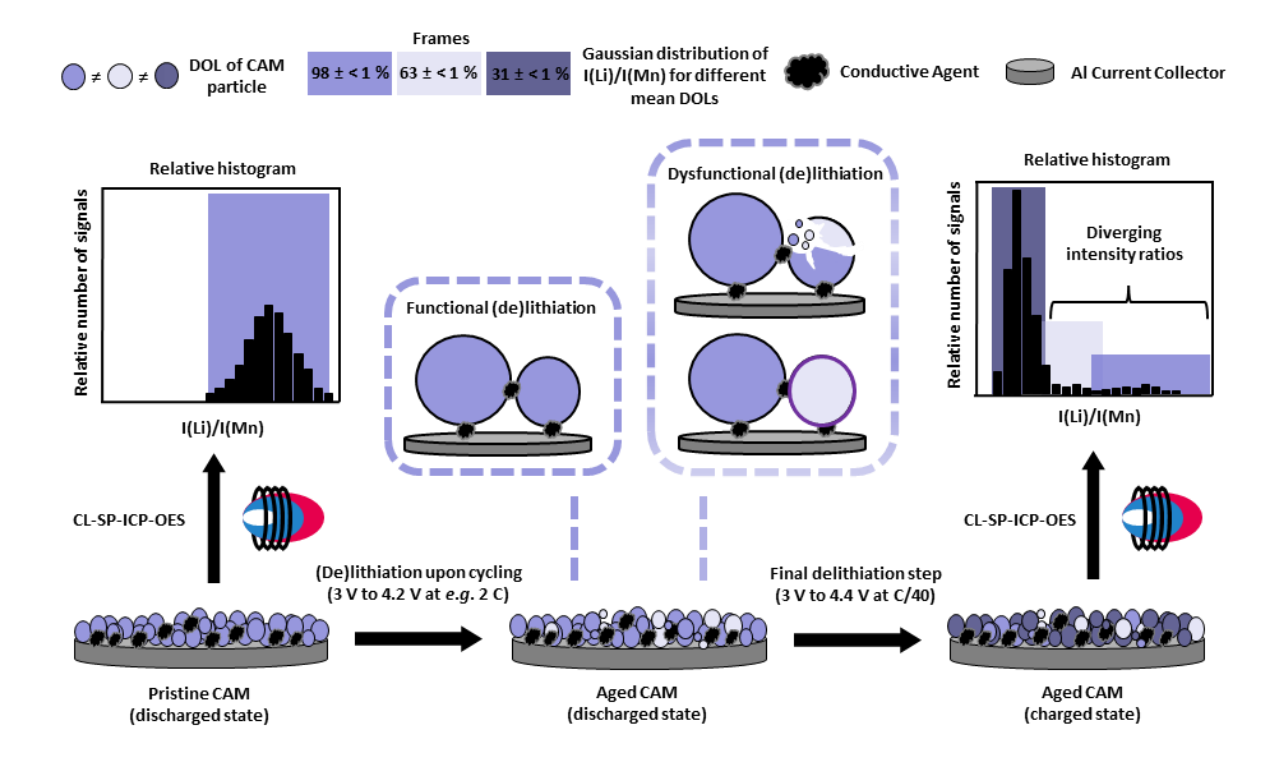
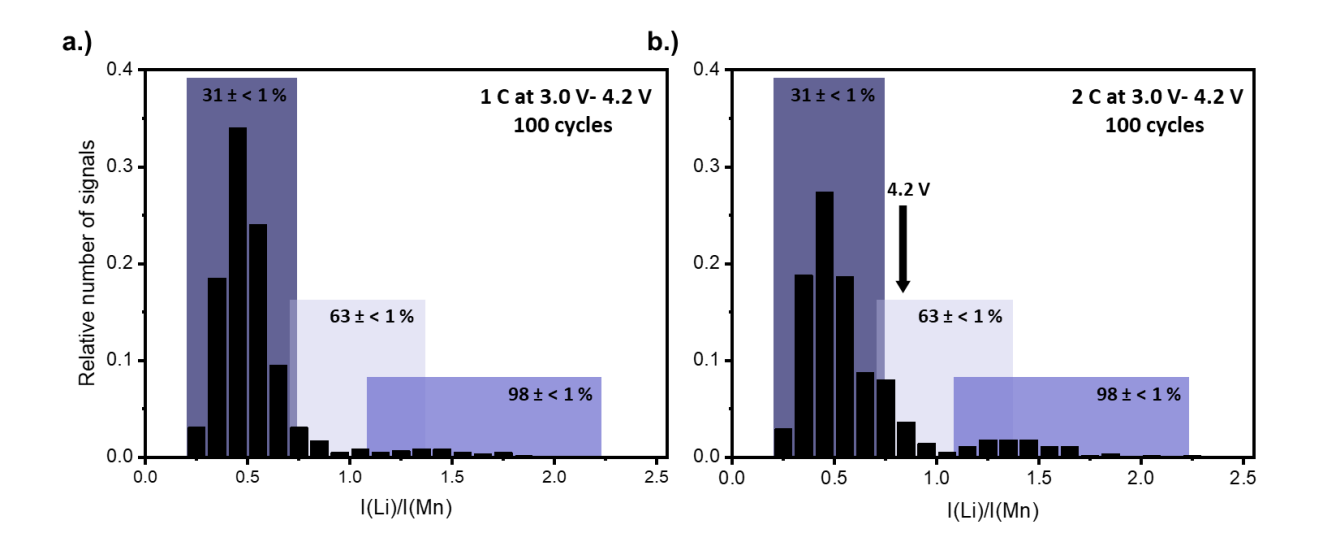


Figure 4. Schematic representation of the design of the CL-SP-ICP-OES experiment.

In **Figure 4**, an explanatory scheme of the design of the CL-SP-ICP-OES experiment is given. As discussed above, the matrix-matched external calibration enables the link of the measured intensity ratios with the DOL of the CAM particles. For this, the Gaussian distributed intensity ratios of the matrix-matched external calibration are presented as frames throughout. After electrochemical cycling, the cells are slowly charged to extract the entire mobile Li from the CAM to a cut-off voltage of 4.4 V as discussed above. The high voltage cut-off criterion is selected to enable the investigation of CAM particles, which potentially lost their electrochemical activity at the cut-off of the cycling voltage window. Under ideal conditions, the mesoscale SOC of the CAM particles corresponds to the macroscale SOC on the electrode level leading to a uniform delithiation during this step. In this case, all the measured intensity ratios are expected to be similar and Gaussian distributed in the frame corresponding to a mean DOL of  $31 \pm < 1$  %. Therefore, the occurrence of diverging intensity ratios outside the frame indicates trapped Li in the CAM, which implies an evolved mesoscale SOC heterogeneity as confirmed by ToF-SIMS. In Figure 5, the relative histograms of the CAM particle intensity ratios after electrochemical cycling and the final charging step in NMC532|graphite cells are presented. It can be observed that after the final delithiation the diverging intensity ratios account for  $8 \pm 1$  % and  $15 \pm 2$  % of the total measured CAM particles for 100 cycles at 1 C and 2 C, respectively. The results show an increase of the diverging intensity ratios and therefore indicate a rate-dependent evolution of the mesoscale SOC heterogeneity upon cycling.



**Figure 5.** Relative histograms of the CAM particle intensity ratios after electrochemical cycling in NMC532 $\parallel$ graphite cells (two-electrode configuration) under different charging protocols at 3.0 V to 4.2 V with a.) 1 C for 100 cycles and b.) 2 C for 100 cycles and a final charging step to a cut-off voltage of 4.4 V as obtained by CL-SP-ICP-OES. Replicate measurements were performed and depicted in the same histograms. The colored frames represent the histograms of the MMEC with a width correlating to the  $\pm$  2  $\sigma$  standard deviation of the corresponding mean intensity ratio.

It can be further observed that the measured intensity ratios are broadly distributed representing fully and partially lithiated CAM particles after delithiation. For the reason that the intensity ratio of Li and Mn is measured, the possibility of a decreased Mn intensity due to *e.g.*, transition metal dissolution (TMD) during cycling needs to be investigated. However, only a very low amount of deposited Mn on the anode was found after cycling and therefore considered as negligible (**Table S-2**). The increase of the SOC heterogeneity after cycling particularly for 2 C implies the occurrence of structural or chemical changes. During high C-rate application, fast and non-uniform (de)lithiation of the CAM is facilitated due to kinetic differences of the Li transport between the particle surface and interior. While the direct exposure of the particle surface to the electrical network enables rapid Li transport, the Li transport flux from the inside of the particles to the outside is slower. Therefore, the particle surface reaches faster the cut-off

potential than the core, which eventually leads to non-uniform capacity utilization of the CAM. Consequently, rate-induced compositional gradients of the Li distribution within the particles and thus unstable structures can result. For layered transition metal oxides, high lithium extraction is accompanied with an intrinsic structural instability leading to the formation of microscopic cracks as shown above. The development of mechanical strain and morphological defects constitute potential physical barriers entailing the disruption of electronic and ionic pathways, which could result in contact loss. <sup>7,17,49,50,53,54</sup> The trapping of Li in disconnected CAM particles could explain the increase of the SOC heterogeneity during cycling. The persistence of trapped Li upon (de)lithiation suggests the immobilization of active Li in electrochemically deactivated CAM particles. <sup>20,33,36</sup> Furthermore, the relative histogram of the CAM particle intensity ratios after cycling for 50 cycles at 2 C exhibits diverging intensity ratios of  $11 \pm 1$  % (**Figure S8**). The increase of the SOC heterogeneity with ongoing cycling further underlines the persistent character of the Li trapping. The occurrence of charged particles at the charging cut-off voltage that might imply increased electrochemical deactivation at high potentials is another important implication of the increased SOC heterogeneity (see Figure 5 b.))<sup>14</sup>. Furthermore, the occurrence of persistent Li deficiency is reported to facilitate the formation of an ionically insulating rock-salt CAM structure leading to increased electrical resistance at the cathode|electrolyte interface.<sup>55</sup> Another possible reason affecting the local electrochemistry pertinent to the cathode electrolyte interface is the formation of the cathode electrolyte interphase (CEI<sup>56</sup>), which begins with the initial wetting of the CAM.<sup>57</sup> Although the complexity of CEI formation is far from being resolved thus far, a thick and non-uniform CEI progression upon prolonged cycling is reported to exasperate the electrochemical performance by further increasing the electrical resistance.<sup>57–60</sup> The resulting mismatch of the local ionic and electronic conductivities can further aggravate the SOC heterogeneity with increasing current density. Therefore, rapid (de)lithiation for accelerated cycling rates is affected by the local chemical and structural heterogeneity in CAMs. For the application of a

moderate cycling rate of 1 C, the heterogeneity of the micro-environment is expected to have less impact due to the more uniform (de)lithiation reactions, which becomes apparent in only a marginal increase of the SOC heterogeneity after cycling. Furthermore, the mesoscale SOC distribution of CAM particles after cycling at 3 C for 100 cycles is investigated. The relative histogram of the CAM particle intensity ratios exhibits diverging intensity ratios of  $10 \pm 1 \%$ (Figure S9), which indicates a decreased SOC heterogeneity contrary to the observed trend at 1 C and 2 C. A possible explanation for this could be that the structural integrity of the polycrystalline particle architecture is severely compromised by the evolution of microscopic cracks at 3 C. In Figure S10, SEM images of FIB-prepared cross-sections of NMC532 electrodes after cycling at 1 C, 2 C and 3 C for 100 cycles are shown. It can be perceived that with the application of a rate of 3 C the extent of particle cracking increases compared to cycling at 2 C leading to the emergence of deep crevices, which expose the particle interior and promote the formation of new electrochemically active surface areas. The evolution of cracks leads to a shortening of lithium transport pathways in the particles and improved charge-transfer kinetics at the cathodelelectrolyte interface possibly bypassing the impact of formed ion-blocking surface films (e.g. rock-salt structures), which compromise the electrochemical activity.<sup>51</sup> Therefore, these results imply that the cracking of polycrystalline particles might not only be detrimental, but could further improve Li transport kinetics resulting in more uniform CAM utilization. 50,51 Furthermore, the results suggest that crack-induced electronic contact loss has a lesser impact on the emerged SOC heterogeneity. However, this benefit is accompanied by increasing the risk of accelerated cathode-electrolyte interfacial degradation. 61 The findings after cycling indicate trapped Li in the CAM, which hints at the occurrence of incomplete electrochemical reactions leading to decreased capacity utilization. Therefore, the capacity loss due to electrochemically inactive Li in the CAM is further investigated by means of a straightforward quantification approach (Figure 6). For this, the amount of active and inactive Li of NMC532 electrodes after cycling is determined after microwave digestion with ICP-OES.

However, as with ICP-OES it is not possible to differentiate between active and inactive Li, additional electrochemical experiments are needed. Therefore, cycled NMC532 electrodes are assembled in NMC532 Li metal cells (two-electrode configuration) to determine the amount of residual active Li during charge (delithiation).

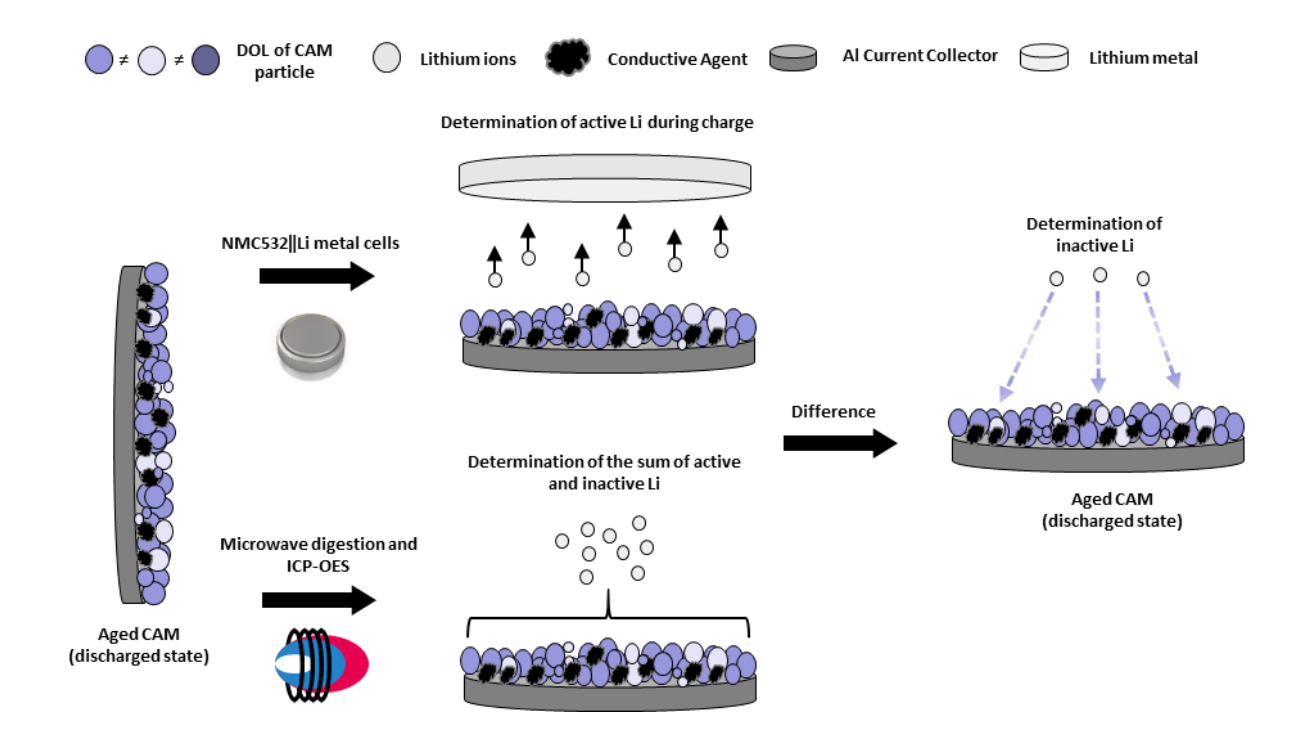


**Figure 6.** Schematic representation for the investigation of inactive Li in the CAM.

The amount of active and inactive Li and the corresponding specific capacity as obtained by ICP-OES and the determined specific charge capacity of the active Li in the experiments with Li metal as the negative electrode are then compared. With this approach, the specific capacity loss corresponding to the amount of inactive Li in the CAM is determined. In **Table 1**, the determined specific capacity loss due to inactive Li in the CAM is presented. The results indicate a rate-dependent change of the determined amount of inactive Li in the CAM. The high standard deviation of the determined capacity loss due to inactive Li might be assigned to the different cells with slightly deviating capacity fading of the replicates used for the cells with Li metal and ICP-OES experiments. In addition, the amount of inactive Li increases from 1 C to 2 C and with ongoing cycling with 2 C, considering the standard deviation. However, the

observed trend does not continue when cycling at 3 C, which is in approximate agreement with the trend of the CL-SP-ICP-OES results. This observation implies a correlation of the determined amount of inactive Li in the CAM with the trapping of Li in electrochemically deactivated particles considering the investigated particle size range with CL-SP-ICP-OES. However, it needs to be emphasized that there are further conceivable reasons contributing to the determined amount of inactive Li. The inactive Li is either located on the surface or within the CAM particles. The occurrence of inactive Li on the particle surface is potentially attributable to the formation of inactive Li species in the course of CEI growth due to spontaneous chemical or electrochemical electrolyte decomposition. <sup>60</sup> The thickness of the CEI is in the nanometer scale<sup>59,62</sup> and therefore considered as negligible compared to the observed electrochemically confined Li reservoirs in individual CAM particles, which sheds new light on existing literature<sup>63</sup>. However, a non-uniform, thick and resistive CEI could contribute to the capacity loss rather by kinetic implications for the transport of the charge carrier as discussed above. Therefore, it is assumed that the determined capacity loss can be assigned predominantly to inactivated Li within the CAM particles, which potentially causes the evolved mesoscale SOC heterogeneity. The charge-discharge cycling performance of the NMC532 graphite cells is given in **Figure S11**.

**Table 1.** Overview of the specific capacity loss due to inactive Li in the CAM as obtained from NMC532||Li metal cells (two-electrode configuration) and after microwave digestion with ICP-OES.

Cycle number	C-rate / C	Inactive Li / mAh g <sup>-1</sup>
100	1	4.5 ± 1.7
50	2	$9.5 \pm 3.4$
100	2	$12.1 \pm 4.4$
100	3	$10.1 \pm 3.4$

The overall capacity fading in **Figure S11** is the sum of the total Li loss in the battery, whereas the determined inactive Li in **Table 1** results only from the capacity loss due to electrochemically inactive Li in the positive electrode. Furthermore, a direct correlation of the results in **Table 1** to the observed capacity fade in **Figure S11** might be difficult due to the different electrochemical conditions of the respective experiments. For the determination of the amount of residual active Li during charge (see **Figure 6**), a lower rate of C/20 was selected to rule out implications from kinetic effects. However, the results of the determined capacity loss related to inactive Li in the CAM indicate a considerable contribution of this Li loss mechanism to the overall capacity fading, which further highlights the need for mesoscopic battery research. The presented methodology of CL-SP-ICP-OES enables this mesoscopic research for the elucidation of the SOC distribution of CAM particles in the electrode and complements the merits of existing analytical techniques (*e.g.* ToF-SIMS).

#### 3. Conclusions

The evolution of persistent mesoscale SOC heterogeneity between different particles was observed upon slow delithiation and extensive relaxation time with CL-SP-ICP-OES. Nanoscale mapping of the Li distribution by means of ToF-SIMS revealed the presence of trapped Li in non- and partially delithiated CAM particles. For particles that were electrochemically inactive from the beginning, the investigation of the local micro-environment suggests the isolation from the ionic and/or electronic network due to structural disintegration during electrode fabrication or deficient contact with conductive agent. For partially delithiated particles, severe micro-cracking in the particle interior was observed, which implies the buildup of kinetic hindrances for the Li and electron transport potentially explaining the heterogeneous Li extraction. However, the micro-cracks also provide more channels for the percolation of electrolyte in the particle interior, which can lead to new electrochemically active surface areas that promote improved Li transport kinetics. Furthermore, it was found that the evolution of SOC heterogeneity observed between different particles is dependent on the current density, with increasing heterogeneity from 1 C to 2 C as obtained by CL-SP-ICP-OES. The observation that the trend is not continuing when cycling at 3 C indicates a potential positive correlation of the degree of micro-cracking with improved Li transport kinetics leading to more uniform CAM utilization. The relationship of the evolved SOC heterogeneity of the particles arising from incomplete electrochemical reactions with decreased capacity utilization was investigated with a straightforward quantification approach. The results reveal a considerable contribution to capacity fading by persistently inactive Li in the CAM, which highlights the importance of the investigation of the mesoscale SOC heterogeneity as a potential capacity fade mechanism in layered oxides. The applied CL-SP-ICP-OES methodology aims to leverage mesoscopic research of the SOC heterogeneity to inform the engineering of CAM particles and electrode formulations for fast-charging and durable batteries.

#### 4. Experimental

#### 4.1. Electrochemical cycling

The cells investigated in this study, were in-house prepared 2032-type coin cells (two-electrode configuration) and Swagelok-type T-cells (three-electrode configuration).<sup>64</sup> The cell chemistry of the NMC532 graphite cells (two-electrode and three-electrode configuration) was based on commercial NMC532 as positive electrode material and SG-3 graphite SGL Carbon SE (Germany) as negative electrode active material. The organic solvent-based electrode preparation of the NMC532 used polyvinylidene difluoride (PVdF) from Solvay (Belgium) as binder dissolved in N-Methyl-2-pyrrolidone (NMP) from Sigma Aldrich (USA) with SuperC65 as conductive agent from Imerys (France). The negative electrode consisted further of styrene-butadiene-rubber (SBR) from Polymer Latex GmbH (Germany) and sodium carboxymethyl cellulose from Dow Wolff Cellulosics (Germany) as binder with deionized water as solvent. Furthermore, SuperC65 from Imerys (France) was used as conductive agent for the negative electrode. As separator, Celgard® 2500 polypropylene foil from Celgard (USA) is used and 1 M LiPF<sub>6</sub> in ethylene carbonate/ethyl methyl carbonate (EC/EMC, (30/70 wt%) from BASF (Germany) was selected as electrolyte. Li metal from Albemarle Corporation (USA) was used as negative electrode in NMC532 Li metal cells (two-electrode configuration) and as reference electrode in the NMC532|graphite cells (three-electrode configuration). The cycling experiments were performed with a 4000 Battery Tester from Maccor (USA).

The electrochemical procedure of the matrix-matched external calibration consisted of a constant current-constant voltage (CCCV) charging step (two-electrode and three-electrode configuration). The NMC532 $\parallel$ graphite cells (two-electrode configuration) were charged to SOCs of 23  $\pm$  2 %, 41  $\pm$  < 1 %, 61  $\pm$  < 1 % and 81  $\pm$  1 % with charge cut-off voltages of 3.6 V, 3.7 V, 4.0 V and 4.4 V at a specific current of 6 mA g<sup>-1</sup>, respectively. The SOC was determined

based on the obtained charge capacity during charge cycling. For this, the theoretical capacity of 278 mAh g<sup>-1</sup> was used as this value represents the absolute Li content. The cut-off voltages have been determined in time limited CC charge cycling experiments with set practical capacities of 56, 111, 167 and 222 mAh g<sup>-1</sup>, respectively.

The electrochemical procedure of the formation for the cycling experiments was comprised of two formation cycles in the voltage range of 3.0 V to 4.2 V at 0.1 C and 0.2 C. The charge-discharge cycling of the NMC532|graphite cells (two electrode configuration) was performed in the voltage range of 3.0 V to 4.2 V with cycling rates of 1 C, 2 C and 3 C. After cycling, the cells were charged to a cut-off voltage of 4.4 V at 6 mA g<sup>-1</sup> for the complete extraction of the mobile Li from the CAM. The NMC532|Li metal cells (two-electrode configuration) were cycled at a cycling rate of C/20 in the voltage range of 3.0 V to 4.22 V. For these experiments, the aged PC-NMC532|graphite cells were disassembled after cycling and the positive electrode was reassembled with Li metal as negative electrode to obtain the residual charge capacity. The specific current at 1 C was defined as 160 mA g<sup>-1</sup> for the cycling experiments.

#### 4.2. ICP-OES investigations

The experimental arrangement and the method development of CL-SP-ICP-OES has been recently published.<sup>35</sup> Therefore, we refer to the detailed experimental information given in that reference and will give only the most important features of the arrangement and analytical method here. The CL-SP-ICP-OES and ICP-OES measurements were performed using the ARCOS from SPECTRO Analytical Instruments GmbH (Germany) with axial plasma viewing. The emission lines of Li 670.776 nm and Mn 257.611 nm were acquired for the analysis of the NMC532. Prior to analysis, the cells were disassembled in dry atmosphere and the NMC532 electrodes were rinsed with 1 ml ethylmethyl carbonate (EMC) and deagglomerated by a heat and ultrasonic treatment in NMP. For this, the UP100H ultrasonic processor from Hielscher

Ultrasonics GmBH (Germany) was used. The deagglomerated particles were then centrifuged and the residue was dried in vacuum for subsequent CL-SP-ICP-OES analysis. For the determination of the residual Li content in the NMC532 after cycling and for the evaluation of the electrochemical delithiation for the matrix-matched external calibration, the electrodes were investigated by acidic microwave digestion and subsequent ICP-OES analysis in solution mode described by Vortmann et  $al^{63}$ . Furthermore, the negative electrodes were investigated in the same manner to examine the potential occurrence of transition metal dissolution after cycling.

#### 4.3. SEM, EDX and ToF-SIMS investigations

Scanning electron microscopy (SEM) was performed using an Auriga CrossBeam workstation from Zeiss (Germany) provided with a field emission gun (Schottky-type) and the energy-dispersive X-ray spectroscopy (EDX) was carried out with an accelerating voltage of 15 kV with an Ultim Extreme EDX detector from Oxford Instruments (United Kingdom). The measurements were performed on multiple areas of the sample. For ToF-SIMS a TOF.SIMS 5 instrument from ION TOF GmbH (Germany) was used. The preparation of the cross section was carried out with focused ion beam (FIB) milling by means of a liquid metal gallium ion source. The analysis of the cross section was performed using a liquid metal bismuth ion source (Bi<sup>+</sup> 30keV) in the imaging mode combined with delayed secondary ion extraction. Before SEM, EDX and ToF-SIMS analysis, the cells were disassembled in dry atmosphere and the electrodes were rinsed with 1 mL EMC.

#### **Conflict of interest**

There are no conflicts to declare.

### Acknowledgements

The authors would like to acknowledge the Ministry of Economic Affairs, Innovation, Digitalization and Energy of the state North-Rhine-Westphalia for funding the project "KWK Projekt Plus Speicher (PRO 0067 A-E)".

#### References

- [1] Wei, C., Xia, S., Huang, H., Mao, Y., Pianetta, P., Liu, Y. Acc. Chem. Res. **2018**, 51, 2484–2492.
- [2] Arinicheva, Y., Wolff, M., Lobe, S., Dellen, C., Fattakhova-Rohlfing, D., Guillon, O., Böhm, D., Zoller, F., Schmuch, R., Li, J., Winter, M., Adamczyk, E., Pralong, V. *Elsevier Series on Advanced Ceramic Materials*. **2020**, 549-709.
- [3] Schmuch, R., Wagner, R., Hörpel, G., Placke, T. Winter, M. *Nat. Energy* **2018**, 3, 267–278.
- [4] Liu, Y., Meirer, F., Krest, C. M., Webb, S., Weckhuysen, B. M. *Nat. Commun.* **2016**, 7, 12634.
- [5] Lin, F., Nordlund, D., Markus, I. M., Weng, T. C., Xin, H. L., Doeff, M. M. *Energy Environ. Sci.* **2014**, 7, 3077–3085.
- [6] Noh, H. J., Youn, S., Yoon, C. S., Sun, Y. K. J. Power Sources **2013**, 233, 121–130.
- [7] Börner, M., Horsthemke, F., Kollmer, F., Haseloff, S., Friesen, A., Niehoff, P., Nowak, S., Winter, M., Schappacher, F. M. *J. Power Sources* **2016**, 335, 45–55.
- [8] Hausbrand, R., Cherkashinin, G., Ehrenberg, H., Gröting, M., Albe, K., Hess, C., Jaegermann, W. *Mater. Sci. Eng. B Solid-State Mater. Adv. Technol.* **2015**, 192, 3–25.
- [9] Vetter, J., Novák, P., Wagner, M. R., Veit, C., Möller, K. C., Besenhard, J. O., Winter, M., Wohlfahrt-Mehrens, M., Vogler, C., Hammouche, A. J. Power Sources 2005, 147, 269–281.
- [10] Kerlau, M., Marcinek, M., Srinivasan, V., Kostecki, R. M. *Electrochim. Acta* 2007, 52, 5422–5429.
- [11] Nakamura, T., Watanabe, T., Amezawa, K., Tanida, H., Ohara, K., Uchimoto, Y., Ogumi, Z. *Solid State Ionics* **2014**, 262, 66–69.
- [12] Tian, C., Xu, Y., Nordlund, D., Lin, F., Liu, J., Sun, Z., Liu, Y., Doeff, M. **Joule** 2018, 2, 464–477.
- [13] Steiner, J. D., Mu, L., Walsh, J., Rahman, M. M., Zydlewski, B., Michel, F. M., Xin, H.
  L., Nordlund, D., Lin, F. ACS Appl. Mater. Interfaces 2018, 10, 23842–23850.

- [14] Lin, F., Markus, I. M., Nordlund, D., Weng, T. C., Asta, M. D., Xin, H. L., Doeff, M. M. Nat. Commun. 2014, 5, 3529.
- [15] Zhang, K., Ren, F., Wang, X., Hu, E., Xu, Y., Yang, X. Q., Li, H., Chen, L., Pianetta, P., Mehta, A., Yu, X., Liu, Y. *Nano Lett.* 2017, 17, 7782–7788.
- [16] Xu, Y., Hu, E., Zhang, K., Wang, X., Borzenets, V., Sun, Z., Pianetta, P., Yu, X., Liu, Y., Yang, X. Q., Li, H. ACS Energy Lett. 2017, 2, 1240–1245.
- [17] Hu, E., Wang, X., Yu, X., Yang, X. Q. Acc. Chem. Res. 2018, 51, 290–298.
- [18] Winter, M., Barnett, B., Xu, K. Chem. Rev. 2018, 118, 11433–11456.
- [19] Tian, C., Nordlund, D., Xin, H. L., Xu, Y., Liu, Y., Sokaras, D., Lin, F., Doeff, M. M. *J. Electrochem. Soc.* **2018**, 165, 696–704.
- [20] Gent, E. W., Li, Y.; Ahn, S., Lim, J., Liu. Y., Wise, A. M., Gopal, C. B., Mueller, D. N., Davis, R., Weker, J., N., Park, J.-H., Doo, S.-K., Chueh, W. C. Adv. Energy Mater. 2016, 28, 6631-6638.
- [21] Wei, C., Zhang, Y., Lee, S. J., Mu, L., Liu, J., Wang, C., Yang, Y., Doeff, M., Pianetta, P., Nordlund, D., Du, X. W., Tian, Y., Zhao, K., Lee, J. S., Lin, F., Liu, Y. J. Mater. Chem. A 2018, 6, 23055–23061.
- [22] Tian, C., Xu, Y., Kan, W. H., Sokaras, D., Nordlund, D., Shen, H., Chen, K., Liu, Y., Doeff, M. ACS Appl. Mater. Interfaces 2020, 12, 11643–11656.
- [23] Mu, L., Lin, R., Xu, R., Han, L., Xia, S., Sokaras, D., Steiner, J. D., Weng, T. C., Nordlund, D., Doeff, M. M., Liu, Y., Zhao, K., Xin, H. L., Lin, F. Nano Lett. 2018, 18, 3241–3249.
- [24] Alvarado, J., Wei, C., Nordlund, D., Kroll, T., Sokaras, D., Tian, Y., Liu, Y., Doeff, M. M. Mater. Today 2019, 35, 87-98.
- [25] Yu, Y. S., Kim, C., Liu, Y., Van Der Ven, A., Meng, Y. S., Kostecki, R., Cabana, *J. Adv. Energy Mater.* **2015**, 5, 1–8.
- [26] Meirer, F., Cabana, J., Liu, Y., Mehta, A., Andrews, J. C., Pianetta, P. J. *Synchrotron Radiat.* **2011**, 18, 773–781.
- [27] Xia, S., Mu, L., Xu, Z., Wang, J., Wei, C., Liu, L., Pianetta, P., Zhao, K., Yu, X., Lin, F., Liu, Y. Nano Energy 2018, 53, 753–762.

- [28] Yabuuchi, N., Makimura, Y., Ohzuku, T. J. *Electrochem. Soc.* **2007**, 154, 314-321.
- Yoon, W. S., Balasubramanian, M., Chung, K. Y., Yang, X. Q., McBreen, J., Grey, C.
  P., Fischer, D. A. J. Am. Chem. Soc. 2005, 127, 17479-17487.
- [30] Gu, M., Belharouak, I., Genc, A., Wang, Z., Wang, D., Amine, K., Gao, F., Zhou, G., Thevuthasan, S., Baer, D. R., Zhang, J. G., Browning, N. D., Liu, J., Wang, C. *Nano Lett.* 2012, 12, 5186–5191.
- [31] Devaraj, A., Gu, M., Colby, R., Yan, P., Wang, C. M., Zheng, J. M., Xiao, J., Genc, A., Zhang, J. G., Belharouak, I., Wang, D., Amine, K., Thevuthasan, S. *Nat. Commun.* **2015**, 6, 8014.
- [32] Lin, F., Nordlund, D., Li, Y., Quan, M. K., Cheng, L., Weng, T. C., Liu, Y., Xin, H. L., Doeff, M. M. *Nat. Energy* **2016**, 1.
- [33] Sui, T., Song, B., Dluhos, J., Lu, L., Korsunsky, A. M. *Nano Energy* **2015**, 17, 254–260.
- [34] Bessette, S., Paolella, A., Kim, C., Zhu, W., Hovington, P., Gauvin, R., Zaghib, K. *Sci. Rep.* **2018**, 8, 1–9.
- [35] Kröger, T.-N., Wiemers-Meyer, S., Harte, P., Winter, M., Nowak, S. *Anal. Chem.* **2021**, 93, 7532-7539.
- [36] Holtstiege, F., Wilken, A., Winter, M., Placke, T. Phys. Chem. Chem. Phys. **2017**, 19, 25905–25918.
- [37] Zhu, L., Bao, C., Xie, L., Yang, X., Cao, X., J. Alloys Compd. 2020, 831, 154864.
- [38] Qi, X., Blizanac, B., Dupasquier, A., Oljaca, M., Li, J., Winter, M. *Carbon N.* Y. **2013**, 64, 334–340.
- [39] Shaju, K. M., Subba Rao, G. V., Chowdari, B. V. R. J. Electrochem. Soc. 2004, 151, 1324-1332.
- [40] Wei, Y., Zheng, J., Cui, S., Song, X., Su, Y., Deng, W., Wu, Z., Wang, X., Wang, W., Rao, M., Lin, Y., Wang, C., Amine, K., Pan, F. J. Am. Chem. Soc. 2015, 137, 8364–8367.
- [41] Deline, V. R., Katz, W., Evans, C. A., Williams, P. Appl. Phys. Lett. 1978, 33, 832–835.
- [42] Priebe, A., Barnes, J. P., Edwards, T. E. J., Huszár, E., Pethö, L., Michler, J. Anal. Chem. 2020, 92, 12518–12527.

- [43] Amin, R., Chiang, Y.-M. J. Electrochem. Soc. 2016, 163, 1512–1517.
- [44] Du, Z., Li, J., Wood, M., Mao, C., Daniel, C., Wood III, D. L. *Electrochim. Acta*, **2018**, 270, 54-61.
- [45] Striebel, K. A., Sierra, A., Shim, J., Wang, C. W., Sastry, A. M. J. Power Sources **2004**, 134, 241–251.
- [46] Daemi, S. R., Lu, X., Sykes, D., Behnsen, J., Tan, C., Palacios-Padros, A., Cookson, J., Petrucco, E., Withers, P. J., Brett, D. J. L., Shearing, P. R. *Mater. Horizons* **2019**, 6, 612–617.
- [47] Yan, P., Zheng, J., Gu, M., Xiao, J., Zhang, J. G. & Wang, C. M. *Nat. Commun.* **2017**, 8, 1–9.
- [48] Lim, J. M., Hwang, T., Kim, D., Park, M. S., Cho, K., Cho, M. Sci. Rep. **2017**, 7, 2–11.
- [49] Liu, H., Wolf, M., Karki, K., Yu, Y. S., Stach, E. A., Cabana, J., Chapman, K. W., Chupas, P. J. Nano Lett. 2017, 17, 3452–3457.
- [50] Trevisanello, E., Ruess, R., Conforto, G., Richter, F. H., Janek, J. Adv. Energy Mater. 2021, 11, 2003400.
- [51] Ruess, R., Schweidler, S., Hemmelmann, H., Conforto, G., Bielefeld, A., Weber, D. A., Sann, J., Elm, M. T., Janek, J. J. *Electrochem. Soc.* **2020**, 167, 100532.
- [52] Ryu, H. H., Park, K. J., Yoon, C. S., Sun, Y. K. Chem. Mater., 2018, 30 1155–1163.
- [53] Song, B., Sui, T., Ying, S., Li, L., Lu, L., Korsunsky, A. M. J. *Mater. Chem.* **2015**, 3, 18171–18179.
- [54] Zhao, K., Pharr, M., Vlassak, J. J., Suo, Z. J. Appl. Phys. **2010**, 108, 1-7.
- [55] Jung, S. K., Gwon, H., Hong, J., Park, K. Y., Seo, D. H., Kim, H., Hyun, J., Yang, W., Kang, K. *Adv. Energy Mater.* **2014**, 4, 1–7.
- [56] Gallus, D. R., Wagner, R., Wiemers-Meyer, S., Winter, M., Cekic-Laskovic, I. *Electrochim. Acta* **2015**, 184, 410–416.
- [57] Li, W., Dolocan, A., Oh, P., Celio, H., Park, S., Cho, J., Manthiram, A. Nat. Commun. 2017, 8, 14589.
- [58] Xiao, B., Sun, X. Adv. Energy Mater. **2018**, 8, 1802057.

- [59] Qian, Y., Niehoff, P., Börner, M., Grützke, M., Mönnighoff, X., Behrends, P., Nowak,S., Winter, M., Schappacher, F. M. *J. Power Sources* 2016, 329, 31–40.
- [60] Xu, K. Chem. Rev. 2014, 114, 11503–11618.
- [61] Cabana, J., Kwon, B. J., Hu, L. Acc. Chem. Res. 2018, 51, 299–308.
- [62] Niehoff, P., Winter, M. Langmuir 2013, 29, 15813–15821.
- [63] Vortmann-Westhoven, B., Winter, M., Nowak, S. J. Power Sources 2017, 346, 63–70.
- [64] Nölle, R., Beltrop, K., Holtstiege, F., Kasnatscheew, J., Placke, T., Winter, M. *Mater*. *Today* **2020**, 32, 131–146.